

## RD\_Mucol/LNF 2023

C. Cantone, A. Cemmi (Associata), F. Colao (Associato), E. Di Meo (Dottoranda),  
I. Di Sarcina (Associata), E. Diociaiuti, P. Gianotti, I. Sarra (Responsabile Locale),  
J. Scifo (Associata), R. Soleti (Associato), A. Verna (Associato)

in collaboration with “LNF-SEA”: S. Ceravolo (Tecnico)  
the Detectors Development and Construction Unit: A. Russo (Tecnico)  
and the BTF team.

In the prospective TeV-scale Muon Collider, the primary hurdle in designing detectors and devising event reconstruction algorithms is the challenge posed by Beam-Induced Background (BIB). Nevertheless, it is conceivable to mitigate the impact of BIB on the Muon Collider’s calorimeter by capitalizing on certain characteristics and ensuring key features such as high granularity, precise timing, longitudinal segmentation, and superior energy resolution. This is what the here described R&D is trying to achieve with an innovative semi-homogeneous electromagnetic calorimeter constructed from stackable and interchangeable modules composed of lead fluoride crystals ( $\text{PbF}_2$ ). These modules are equipped with surface-mount UV-extended Silicon Photomultipliers (SiPMs) and are collectively referred to as the Crilin calorimeter (CRystal calorImeter with Longitudinal INformation). The challenge lies in making sure this calorimeter can operate effectively within an extremely harsh radiation environment, enduring an annual neutron flux of  $10^{14} n_{1\text{MeV}}/\text{cm}^2$  and a total ionizing dose of 10 kGy. In this paper, the radiation tolerance measured in several irradiation campaigns is discussed. Additionally, reflecting on the impressive results of a dedicated test beam conducted at CERN H2 in August 2022 on a single-cell prototype, employing a 120 GeV electron beam, the achievement of a timing resolution of less than 50 ps for energy deposits exceeding 1 GeV underscores the robustness of the system. Subsequently, a larger prototype (Proto-1), comprising two layers of 3x3  $\text{PbF}_2$  crystals each, underwent testing in 2023. These tests were conducted using 500 MeV electrons at the LNF Beam Test Facility and with 40-150 GeV electrons at CERN H2. Detailed information on the prototype’s mechanics and electronics, along with the outcomes of the test beams, is presented for consideration.

### 1 Radiation hardness

Because of the BIB, a highly challenging environment is anticipated for the Muon Collider. As a result, a FLUKA [1] simulation at  $\sqrt{s} = 1.5$  TeV was conducted, with the aim to determine the Total Ionizing Dose (TID) and neutron fluence levels expected on the whole detector interface. For the ECAL barrel region, the expected neutron fluence and dose are  $10^{14} n_{1\text{MeV}}/\text{cm}^2$  per year and a total ionizing dose of 10 kGy per year, respectively. So once the radiation levels were determined, it was necessary to assess the radiation tolerance of individual components of the calorimeter and explore various options. Starting with crystals, for Crilin, as anticipated, the baseline choice is represented by  $\text{PbF}_2$ . Additionally,  $\text{PbWO}_4$ -UF [2] emerges as a viable candidate. This material possesses high density, a good light yield, radiation resistance and a high response speed due to its combination of prompt Cherenkov and a fast scintillation component. It exhibits a dominant emission with a decay time of less than 700 ps. To assess the radiation resistance of both crystals, a Total Ionizing Dose (TID) irradiation campaign was conducted, following a preliminary campaign in 2021 [3]. The irradiation was carried out at the ENEA-Calliope facility using  $^{60}\text{Co}$  source. The transmittance measurements were performed along the crystal axis (longitudinally) using a

PerkinElmer Lambda 950 UV/VIS dual-beam spectrometer. In this case the optical transmittance has been evaluated as follows:

$$T = \frac{\frac{S-D}{Ref-D}}{\frac{S_0-D_0}{Ref_0-D_0}},$$

where  $S$ ,  $D$  and  $Ref$  are respectively the measured, dark and reference signals, while the subscript 0 refers to the baseline measurement performed without the crystal inside the spectrometer.

The resulting transmittance spectra after irradiation are shown in Figure 1 for the two different crystals having the same dimensions ( $1 \times 1 \times 4 \text{ cm}^3$ ). Notably, after a TID exceeding 350 kGy, a not substantial decrease in transmittance was observed for  $\text{PbF}_2$ , which also held true for  $\text{PbWO}_4\text{-UF}$  up to 1 MGy. The results are also compatible with the one observed in [4] and [5]. A second irradiation campaign was conducted to assess the radiation hardness of the SiPMs at the Frascati Neutron Generator (FNG-ENEA) facility using 14 MeV neutrons with a fluence of up to  $10^{14} \text{ n}_{1\text{MeV}}/\text{cm}^2$ . Neutron irradiation is a significant concern when using these sensors, as it leads to a notable increase in dark current. Two series of SiPMs were tested: one with a pixel size of  $15 \mu\text{m}$  and another with a pixel size of  $10 \mu\text{m}$  (models SMD S14160-3015PS and S14160-3010PS). The reference value before irradiation are presented in Table 1. By measuring the dark current after irradiation at three different temperatures (results summarized in Table 2 and Table 3 respectively), it became evident that the optimal choice for SiPM pixel size to withstand the radiation environment of the Muon Collider is the  $10 \mu\text{m}$  size, as it exhibits a less concerning dark current increase.

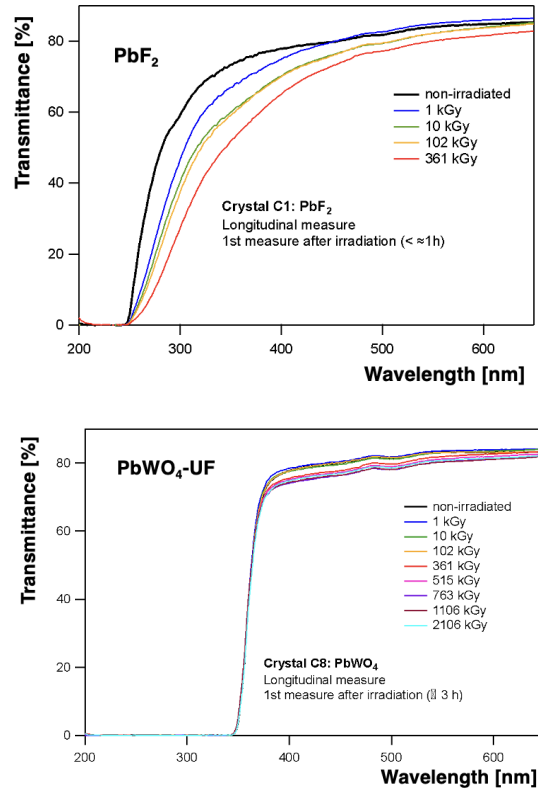


Figure 1: Transmission spectra obtained in the different irradiation steps for the  $\text{PbF}_2$  (top) and  $\text{PbWO}_4\text{-UF}$  (bottom) crystal samples (with same dimensions  $1 \times 1 \times 4 \text{ cm}^3$ ).

Table 1: Breakdown voltage and operational currents for both SiPMs before irradiation at 25°C

SiPM pixel-size	$V_{br}$ [V]	$I(V_{br}+4V)$ [nA]	$I(V_{br}+6V)$ [nA]	$I(V_{br}+8V)$ [nA]
15 $\mu m$	78.00 $\pm$ 0.01	35.03 $\pm$ 0.01	80.50 $\pm$ 0.01	152.35 $\pm$ 0.01
10 $\mu m$	80.97 $\pm$ 0.01	23.89 $\pm$ 0.01	42.58 $\pm$ 0.01	70.80 $\pm$ 0.01

Table 2: Breakdown voltage and currents for the 15  $\mu m$  SiPM after irradiation at different temperatures.

T [°C]	$V_{br}$ [V]	$I(V_{br}+4V)$ [mA]	$I(V_{br}+6V)$ [mA]	$I(V_{br}+8V)$ [mA]
-10 $\pm$ 1	75.29 $\pm$ 0.01	12.56 $\pm$ 0.01	30.45 $\pm$ 0.01	46.76 $\pm$ 0.01
-5 $\pm$ 1	75.81 $\pm$ 0.01	14.89 $\pm$ 0.01	32.12 $\pm$ 0.01	46.77 $\pm$ 0.01
0 $\pm$ 1	76.27 $\pm$ 0.01	17.38 $\pm$ 0.01	33.93 $\pm$ 0.01	47.47 $\pm$ 0.01

Table 3: Breakdown voltage and currents for the 10  $\mu m$  SiPM after irradiation at different temperatures.

T [°C]	$V_{br}$ [V]	$I(V_{br}+4V)$ [mA]	$I(V_{br}+6V)$ [mA]	$I(V_{br}+8V)$ [mA]
-10 $\pm$ 1	76.76 $\pm$ 0.01	1.84 $\pm$ 0.01	6.82 $\pm$ 0.01	29.91 $\pm$ 0.01
-5 $\pm$ 1	77.23 $\pm$ 0.01	2.53 $\pm$ 0.01	9.66 $\pm$ 0.01	37.51 $\pm$ 0.01
0 $\pm$ 1	77.49 $\pm$ 0.01	2.99 $\pm$ 0.01	11.59 $\pm$ 0.01	38.48 $\pm$ 0.01

## 2 Proto-1

The innovative concept behind the Crilin ECAL involves utilizing multiple layers of  $PbF_2$  crystals along with thin surface-mount device (SMD) SiPMs stacked on top of each other to provide longitudinal information about the shower. To validate these design choices, a larger prototype, known as Proto-1, was recently constructed. The Proto-1 (Figure 2) design underwent optimization through simulation studies, starting with transverse and longitudinal dimensions of 0.7  $R_M$  and 8.5  $X_0$  (0.3 $\lambda$ ) respectively. It consists of two layers of 3 $\times$ 3  $PbF_2$  crystals each readout by two series of two UV-extended SiPMs. This size was chosen as a compromise between achieving acceptable containment of approximately 100 GeV electron showers and adhering to cost constraints. The obtained results will be extrapolated to determine the optimum length for the Muon Collider calorimeter, which is expected to be on the order of 20 radiation lengths ( $X_0$ ). Two stackable and interchangeable submodules, assembled by bolting, house the crystals. Furthermore, the light-tight case also incorporates the front-end electronic boards and cooling system. Indeed, the on-detector electronics and SiPMs must be cooled during operation to enhance and stabilize the performance of SiPMs against irradiation. This design effectively removes the heat load resulting from the increased photo-sensor leakage current after exposure to the expected fluence of  $10^{14}$   $n_{1MeV}/cm^2$ . The total heat load was estimated to be 350 mW per channel. The Crilin cooling system consists of a cooling plant and a cold plate heat exchanger made of copper, which is mounted directly over the electronic board. A glycol-based water solution flows through deep-drilled channels, absorbing the heat generated by the SiPMs. This setup ensures the optimum operating temperature for the electronics and SiPMs, which is maintained at 0/-10°C.

The prototype Front-End Electronics (FEE), regulating a single module, is divided into two main parts (Figure 3): a SiPM board and a corresponding Mezzanine board. Each SiPM board, as



Figure 2: Proto-1 images: a single module during crystal (with a Mylar wrapping) installation, the locking system of the two layers together with the heat exchanger and finally the prototype fully assembled.

shown in Figure 3-left, contains 36 photo-sensors, allowing each crystal in the matrix to have two separate and independent readout channels. These channels consist of two  $10\ \mu\text{m}$  pixel-size SMD S14160-3010PS SiPMs [7], selected for their high-speed response, narrow signals, and radiation hardness. Additionally, four SMD blue LEDs are placed between the SiPM matrices to perform in-situ calibration, diagnostics, and monitoring. The SiPMs are connected via  $50\ \Omega$  micro-coaxial transmission lines to a microprocessor-controlled Mezzanine Board. The Mezzanine Board oversees signal amplification and shaping, as well as all slow control functions for all the 18 readout channels of the single layer. The SiPMs' biasing is controlled by 12-bit DACs, and regulated voltages, bias currents, and the temperature of the SiPM matrix are sensed through dedicated 12-bit ADC channels. The slow control routines are then managed by an onboard Cortex M4 microprocessor.

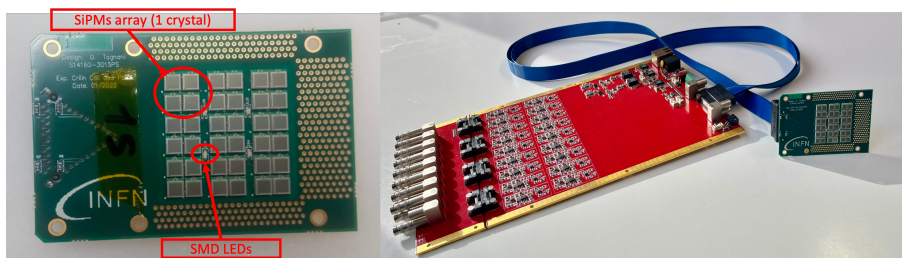


Figure 3: FEE parts: on the left-hand side the SiPMs board embedding the 36 photo-sensors, 4 for each crystal, and 4 blue-LEDs needed for diagnostic and in-situ calibration. On the right-hand side the Mezzanine board that bias, regulate and readout a single SiPMs board, connected through  $50\ \Omega$  micro-coaxial transmission lines.

### 3 BTF beam test

One of the first test-benches for Proto-1 consisted in a low-energy beam test at LNF-Beam Test Facility (BTF), carried out in collaboration with the KLEVER/Na62 group. The Beam Test Facility (BTF) at LNF is part of the DAΦNE accelerator complex and can deliver electron or positron beams with an energy up to 510 MeV. This facility offers the possibility to adjust the beam intensity delivered to the experimental hall, ranging from approximately  $10^{10}$  particles per bunch down to less than a single particle per bunch on average. Moreover the beam spot and position can be fine-tuned using quadrupoles, dipoles, and correctors along the BTF line. Real-

time monitoring of the beam spot and position is conducted using silicon pixel hybrid detectors (FitPix) with an active area of  $14 \times 14 \text{ mm}^2$  and a  $55 \mu\text{m}$  pitch. The aim of this beam test was to evaluate the time resolution performances, to give a first estimation of the energy resolution of the calorimeter and, at the same time, evaluate the most performing crystal wrapping.

### 3.1 Setup

All measurements were carried out with 450 MeV single-electron beam using a dedicated mechanical setup described in the following. The prototype was placed on an 2-axis motorised stage for alignment (Figure 4). An external time reference source was placed in front of Proto-1 and centered with respect to the central crystal thanks to a second motorised stage. The time reference detector consists of a  $2 \times 1 \times 1 \text{ cm}^3$  plastic scintillator, more specifically EJ200, optically coupled on two sides with two R9880U Hamamatsu PMTs. These signals, together with the 36 Proto-1 readout channels, were digitized using a CAEN V1742 Switch Capacitor digitizer operating at 5 Gsps. The acquisition was initiated by the logic coincidence of the two signals discriminated signals from the time reference PMTs (100 mV thresholds) and a trigger embedded in the BTF system. The

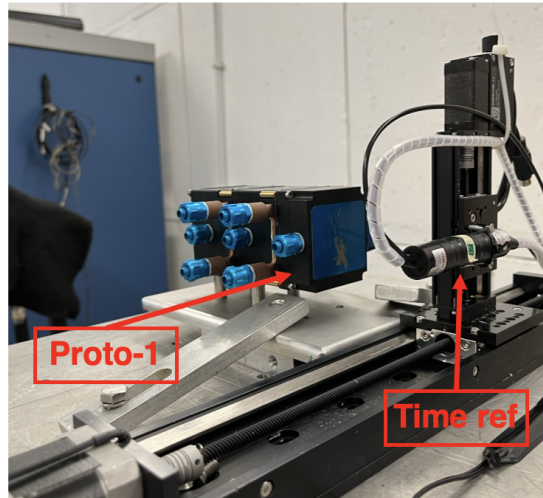


Figure 4: Mechanical setup picture during alignment of the reference scintillator, placed upstream, with the central crystal of Proto-1

scintillator was also used to discriminate single particle events. Indeed once the charges were reconstructed for each event it was possible to identify the interesting events just by applying cuts on the distributions in Figure 5-top. These distributions show two peaks linked to one and two particles events respectively, meaning that by choosing events with  $50 \text{ pC} < Q_{\text{CH0}} < 90 \text{ pC}$  and  $25 \text{ pC} < Q_{\text{CH1}} < 75 \text{ pC}$  single particle events were selected. The time resolution performances of this tagger were also analysed. The pulse time was evaluated in the following way: for each waveform, the timing was extracted by applying a polynomial spline interpolation to the waveform rising edge and peak, using a constant fraction technique (CF) applied to the spline function. The CF value employed for this reconstruction was 5% of the spline peak amplitude, optimised by minimising the resolution on the difference of the two PMTs pulse timings. The same timing method was also employed for Proto-1 signals. The distribution of the time difference  $\Delta T$  between the two channels is presented in Figure 5-bottom: a Gaussian fit was overlaid resulting in a  $\sigma_{\Delta T}$  of  $\sim 107 \text{ ps}$ . The Proto-1  $\text{PbF}_2$  crystals were tested in BTF with two different wrapping configurations, i.e. Mylar

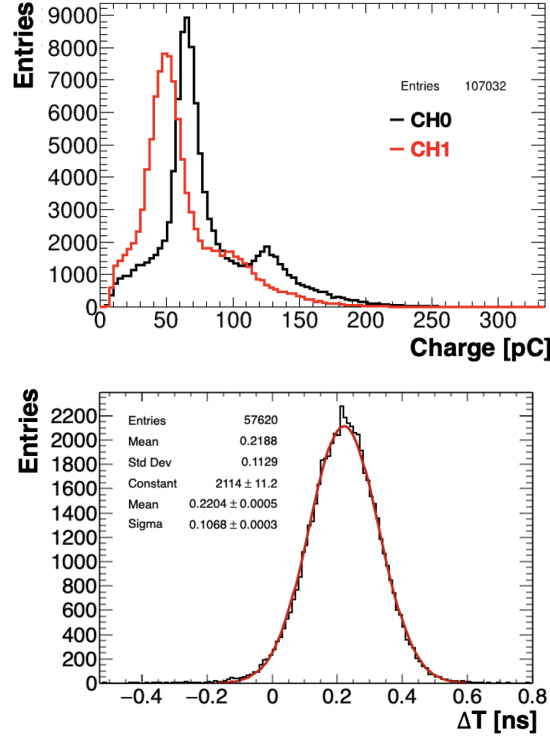


Figure 5: Top panel: charge distributions of the two channels of the scintillating tagger used as single particle events selector and timing reference. Bottom panel: time difference between the two PMTs. A  $\sigma_{\Delta T}$  of  $\sim 107$  ps is derived from the Gaussian fit.

and Teflon. The SiPM biases were set 2V over the nominal operational voltage ( $V_{op}$ ) provided by the vendor. For R&D purposes, one of the readout boards was tested connecting the SiPMs pairs in parallel, differently from the baseline choice (series connection). Note that the upstream layer was always readout by the series-connected board, to better exploit the larger energy deposits in that layer, since the shower peak is expected to be at a depth of  $t_{max} = (\ln(E/E_c) - 1) X_0 = 2.7$  cm [9]. Moreover, as a consequence of [6], all runs were taken in the "back" configuration.

### 3.2 Light output and energy deposit

Proto-1 signals were filtered using a Butterworth second-order low-pass filter with a 500 (250) MHz cut frequency for boards with SiPM in series (parallel), then integrated in the [20, 100(190)] ns window to evaluate the charge, applying a threshold at 2 (5) pC in the reconstruction, while the pulse timing was estimated applying the same method of the reference scintillator but with a different constant fraction value of 11%. The noise on the charge due to the electronics is distributed as a Gaussian function with zero mean and 1 pC standard deviation, as evaluated using pedestal runs where the acquisition was initiated by a random trigger. The ratio between charge and number of photo-electrons is evaluated to be 0.4 pC per photo-electron, as a consequence of a FEE gain of 10 and a SiPM Gain of  $2.5 \times 10^5$  at  $V_{op} + 2V$  bias condition. Geant4 simulations were carried out using a 450 MeV single-electron source. The electrons impinging on the calorimeter were distributed spatially as a 2D Gaussian in the transversal direction. The simulated Gaussian parameters were

set using the information collected with the FitPix provided by BTF resulting in  $(-0.14, -0.04)$  mm mean values and  $(0.66, 0.45)$  mm RMS in the  $x$  and  $y$  coordinates respectively. From the deposited energy distributions generated using Geant4, reconstructed charge distributions were evaluated by taking into account the electronic noise as a Gaussian smearing, the charge/photo-electrons ratio as a scale factor and the Poissonian photo-statistics fluctuations parametrized by the light yield (photo-electrons per unit of deposit energy). The light yield is an input parameter of this procedure and it was fitted by comparing data and MC distributions for the mean charge of the central crystal of each layer. Finally a threshold at 50 MeV was directly applied in the Geant4 simulation. This procedure was repeated for the two wrapping configurations, where  $10^6$  events were generated for each in Geant4. A picture of the prototype simulated geometry is presented in Figure 6 embedding the 2 layers of  $\text{PbF}_2$  crystals and 2 layers of PCB-like material. The MC energy distribution showed

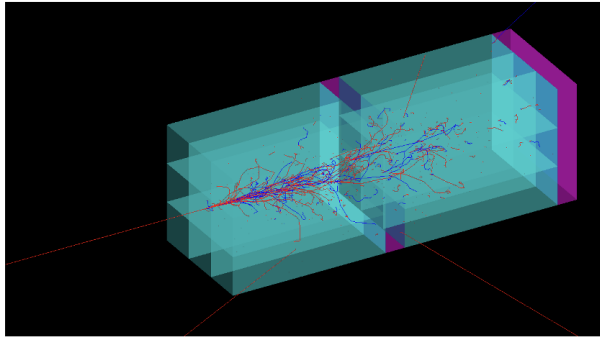


Figure 6: Picture of Proto-1 simulated geometry showing its two layers consisting of 9  $\text{PbF}_2$  crystals each and a PCB-like material simulating the photo-sensors board. The development of one 450 MeV electron shower is also visible.

a most probable energy deposit of about 170 MeV for the central crystal in the front calorimeter layer as shown in Figure 7, to be compared to the analogous mean charge distribution in data that is peaked instead at 25 pC (for the Teflon wrapping). For both wrappings, the histogram of the deposited energy distribution from the MC was fitted on data using normalisation and light yield as parameters. From the fit procedure, light yield values of 0.32 p.e./MeV and 0.25 p.e./MeV were obtained for Teflon and Mylar wrappings respectively. An example of the data-MC overlay for the Teflon case is shown in Figure 8, where the range 15-60 pC was used for the MC shape fit. Focusing on the charge collected by the whole calorimeter, again for the Teflon case, it is possible to observe a mixture of two statistical populations, the lower charge one represents the single-particle events and was fitted with a Gaussian distribution showing a 20% charge resolution, while the second one correspond to a small contamination from two-particle events, as shown in Figure 9. Finally the Proto-1 centroid in X and Y axis was also estimated using the charge information, indeed it was calculated as the average position of the center of the crystals  $(-1, 0, 1)$  cm weighted on the charge of the crystals including both layers. The 2D distribution for the Teflon case is presented in Figure 10 and, show a resolution of  $(0.25, 0.22)$  cm in the X-Y axis, to be compared with the naive  $1/\sqrt{12}$  cm estimable uncertainty, is achieved and it should also be noted that the beam spread contribution to this resolution can be considered negligible.

### 3.3 Time resolution

The time resolution of the central-cell of the prototype was also evaluated during the beam test. Again the performance of the two wrapping choices were compared. The back layers were not

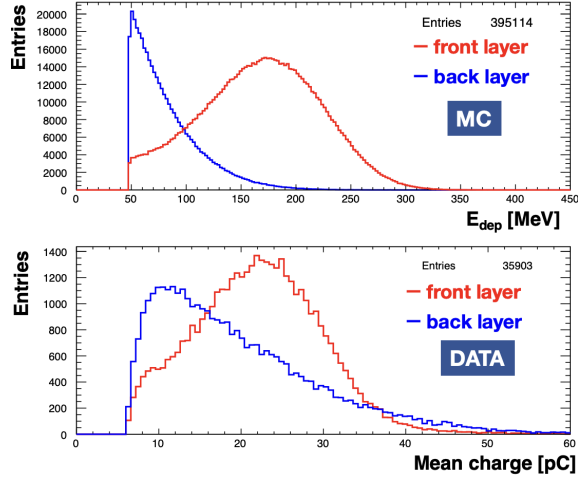


Figure 7: Development of the MC energy distribution (top panel) in the central crystal of both layers compared to the analogous charge distribution in data (bottom panel)

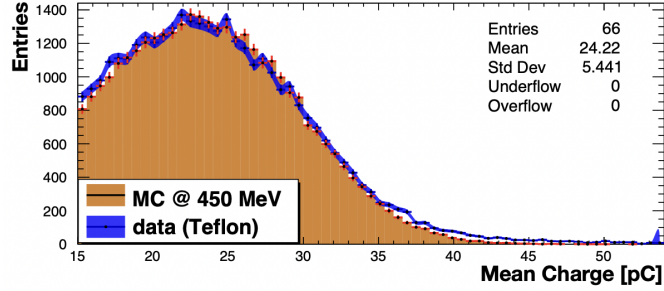


Figure 8: Data-MC consistency test performed by fitting data with the MC energy distribution with the aim to find the optimal scale light yield values, resulting, in the Teflon-wrapping case in Figure, in 0.32 p.e./MeV.

analyzed because the presence of SiPMs in parallel increases the capacitance of a factor 4 with respect to the series case, hence worsening the signals shapes and time resolution as well. Starting from the distribution of the  $\Delta T$  as a function of the mean charge collected in the crystal, the time resolution,  $\sigma_{\Delta T}/2$ , was then estimated from Gaussian distribution fits applied to 10 energy deposition ( $E_{dep}$ ) slices. The resulting plots, for the two different wrappings, are summarised in Figure 11. As in [6], the time resolution distribution was fitted using the formula,

$$\sigma_{MT} = \frac{\sigma(T_1 - T_0)}{2} = \frac{a}{E_{dep}} \oplus b \quad (1)$$

showing a mean time cell resolution less than 150 ps for energy deposit greater than 40 MeV for both wrappings but, at the same time, the Teflon one displays a lower constant term and a higher energy deposit. Considering the aforementioned results together with the ones in [6], and keeping in mind the high-energy purposes of the calorimeter, the optimal configuration seems to be the one with  $\text{PbF}_2$  with a Teflon wrapping and a readout provided by two series connection of two 10  $\mu\text{m}$  pixel-size SiPMs, all placed in the “back” orientation. For this final configuration

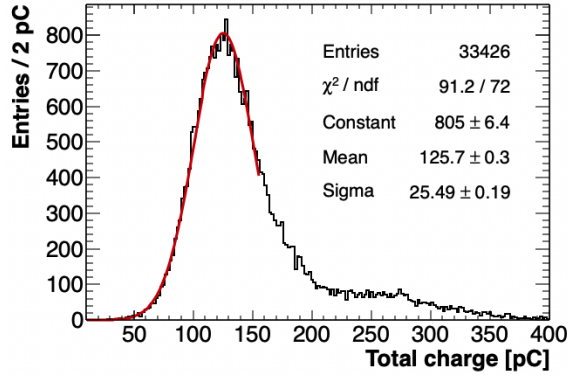


Figure 9: Distribution of the charge collected by the whole calorimeter obtained by summing all the readout channel contribution. A Gaussian fit was applied on the first peak (single-particle) resulting in a relative charge resolution of 20%.

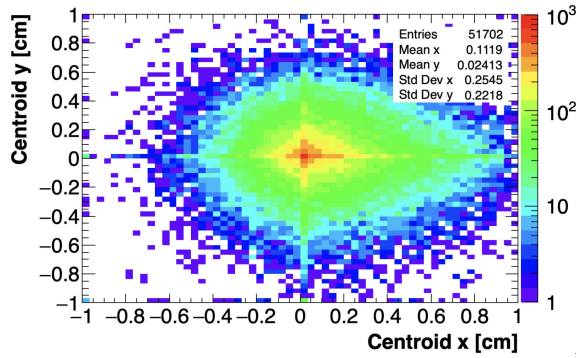


Figure 10: 2D distribution of the Proto-1 centroid at 450 MeV evaluated as average position of the center of the crystals (-1, 0, 1) cm weighted on the charge of the crystals.

the time performances were also evaluated with respect to the external time reference mentioned above from the distribution of the difference between the central-crystal mean time and the external time reference mean time, cutting as before on the single-particle events. The distribution shape in Figure 12 the fits is modelled by a double-sided Crystal Ball (DSCB) function, an empirical function comprising a Gaussian core together with power-law tails on both sides. A time resolution of  $\sim 100$  ps is derived meaning that the central crystal time resolution averaged on all the energy range is  $\sim 100$  ps as well.

#### 4 CERN beam test

In August 2023, a second test beam was conducted at CERN-SPS beamline using electrons with the energies of 40–60–100–120–150 GeV. The test aims to assess the detector's response at high energies. Data analysis is still ongoing, and the results will be presented at the 16th Pisa Meeting on Advanced Detectors and Calor2024 conferences.

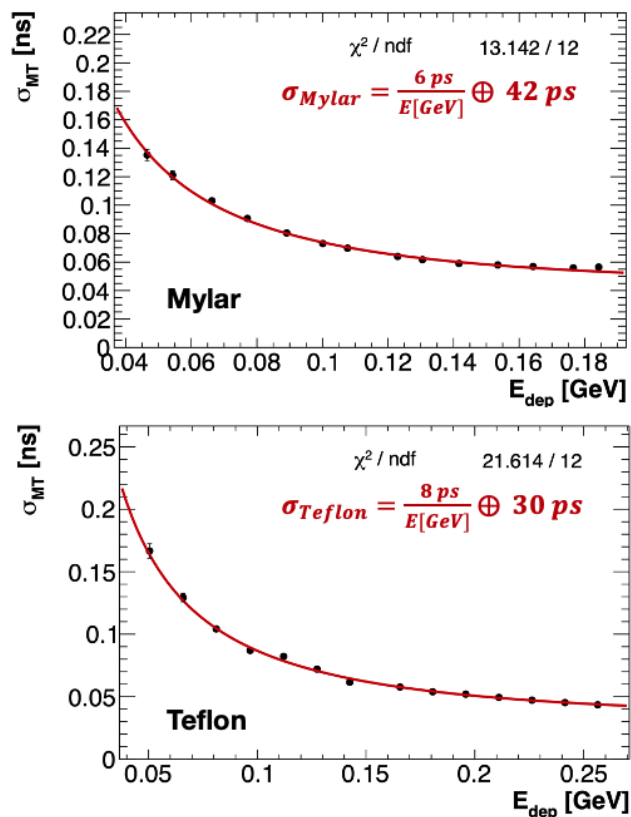


Figure 11: Mean time cell resolution for the central crystal evaluated starting from the  $\Delta T/2$  distribution as a function of the energy deposits for 15 different slices. Both wrapping cases, Mylar in the top panel and Teflon in the bottom one, were fitted accordingly to the 1.

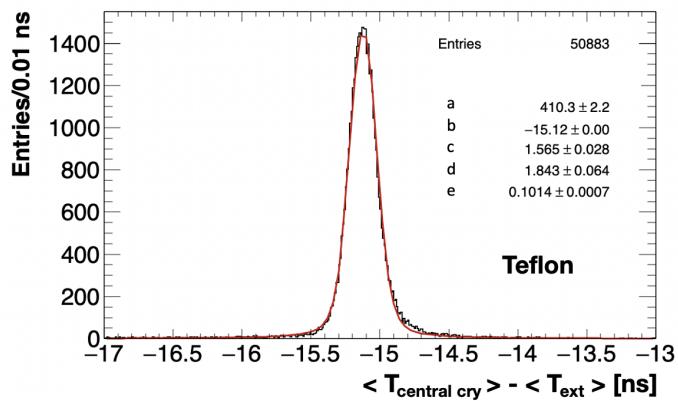


Figure 12: Time resolution evaluated using the external time reference. Using a double-sided Crystal Ball (DSCB) fit a time resolution of  $\sim 100$  ps is derived from the distribution of difference from the central crystal mean time and the time reference mean time.

## 5 List of Conference Talks/Posters by LNF Authors in the Year 2023

1. E. Di Meo, R&D status for an innovative crystal calorimeter for the future Muon Collider, ANIMMA 2023, Lucca, IT.
2. I. Sarra, R&D status for an innovative crystal calorimeter for the future Muon Collider, TIPP 2023, Cape Town, South Africa.

## 6 Publications

- Cantone C, Carsi S, Ceravolo S, Di Meo E, Diociaiuti E, Frank I, et al. Beam test, simulation, and performance evaluation of PbF2 and PWO-UF crystals with SiPM readout for a semi-homogeneous calorimeter prototype with longitudinal segmentation. *Frontiers in Physics* 11 (2023). doi:10.3389/fphy.2023.1223183.
- C. Cantone, et al., "R&D status for an innovative crystal calorimeter for the future Muon Collider", *EPJ Web Conf.* 288 02002 (2023), DOI: 10.1051/epjconf/202328802002.

## References

1. A. Ferrari et al., "FLUKA: a multi-particle transport code", CERN-2005-10 (2005).
2. Korzhik M, et al. Ultrafast PWO scintillator for future high energy physics instrumentation. *Nucl. Instrum. Meth. A* 1034 (2022) 166781. doi:10.1016/j.nima.2022.166781.
3. Cemmi, A., et al. Radiation study of Lead Fluoride crystals. *Journal of Instrumentation* 17.05 (2022): T05015.
4. Guo-Hao Ren, Ding-Zhong Shen, Shao-Hua Wang, and Zhi-Wen Yin. Optical absorption on cubic  $\beta$ -PbF2 crystals. *Chinese Physics Letters*, 18(7):976–978, 2001.
5. Peter Kozma, Robert Bajgar, and Petr Kozma Jr. Radiation resistivity of PbF2 crystals. *Nuclear Instruments and Methods in Physics Research Section A: Accelerators, Spectrometers, Detectors and Associated Equipment*, 484(1-3):149–152, 2002.
6. Cantone C, Carsi S, Ceravolo S, Di Meo E, Diociaiuti E, Frank I, et al. Beam test, simulation, and performance evaluation of PbF2 and PWO-UF crystals with SiPM readout for a semi-homogeneous calorimeter prototype with longitudinal segmentation. *Frontiers in Physics* 11 (2023). doi:10.3389/fphy.2023.1223183.
7. Hamamatsu S14160-3010PS datasheet, [https://www.hamamatsu.com/content/dam/hamamatsu-photonics/sites/documents/99\\_SALES\\_LIBRARY/ssd/s14160-1310ps\\_etc\\_kapd1070e.pdf](https://www.hamamatsu.com/content/dam/hamamatsu-photonics/sites/documents/99_SALES_LIBRARY/ssd/s14160-1310ps_etc_kapd1070e.pdf)
8. Buonomo B, Di Giulio C, Foggetta LG, Valente P. The Frascati LINAC Beam-Test Facility (BTF) Performance and Upgrades. 5th International Beam Instrumentation Conference (2017), TUPG29. doi:10.18429/JACoW-IBIC2016-TUPG29
9. Particle Data Group , P A Zyla, R M Barnett, J Beringer, O Dahl, D A Dwyer, D E Groom, C -J Lin, K S Lugovsky, E Pianori et al. Review of Particle Physics, *Progress of Theoretical and Experimental Physics*, Volume 2020, Issue 8, August 2020, 083C01, <https://doi.org/10.1093/ptep/ptaa104>